Title

A viscoplastic constitutive model for plastic silts and clays for static slope stability applications

Authors

Oathes, Tyler J
Boulanger, Ross W
Ziotopoulou, Katerina

Publication Date

2024

DOI

10.1139/cgj-2022-0479

Peer reviewed

Canadian Geotechnical Journal

Article

A viscoplastic constitutive model for plastic silts and clays for static slope stability applications

Tyler J. Oathes[a], **Ross W. Boulanger**[b], **and Katerina Ziotopoulou**[b]

[a]Department of Civil and Environmental Engineering, Rutgers University, Piscataway, NJ 08854, USA; [b]Department of Civil and Environmental Engineering, University of California, Davis, CA 95616, USA

Corresponding author: **Tyler J. Oathes** (email: tyler.oathes@rutgers.edu)

Abstract

A viscoplastic model for representing plastic silts and clays in geotechnical static slope stability applications is presented. The PM4SiltR model builds on the stress ratio-controlled, critical state-based, bounding surface plasticity model PM4Silt and is coded as a dynamic link library for use in the finite difference program FLAC 8.1. PM4SiltR incorporates strain rate-dependent shear strength, stress relaxation, and creep using a consistency approach combined with an internal strain rate and auto-decay process. The model does not include a cap, and as such cannot simulate strain rate-dependent consolidation under increasing overburden stress. Six parameters control the viscous response for PM4SiltR, while the parameters controlling the nonviscous components of the response are the same as for PM4Silt. Single element simulations are presented to illustrate the influence of viscoplasticity on the constitutive response in direct simple shear loading and undrained creep. Single element responses are shown to be consistent with observed experimental results. Simulations of a hypothetical tailings dam constructed using the upstream method are performed to illustrate use of PM4SiltR at field scale. Results of field-scale simulations show PM4SiltR can model undrained creep and progressive failure leading to delayed slope instability after relatively minor changes in loading conditions at field scale.

Key words: viscoplastic, slope stability, plastic silts and clays, consitutive model

Introduction

Stability and deformation of slopes and embankments comprised in part of saturated, loose-of-critical-state, fine-grained soils are affected by a number of complex mechanisms including potential strain-softening and associated localization, pore pressure diffusion (consolidation), creep, and strength anisotropy. Analyses need to consider drained and undrained conditions and the large range of potential behaviors possible for each drainage condition. Observable behaviors in undrained loading may vary from undrained creep rupture in sensitive clays to static liquefaction in loose silty sands. Rates of pore pressure diffusion during various loading conditions can be difficult to evaluate confidently, particularly in highly heterogeneous deposits or hydraulically placed fills. The timing of a delayed slope instability after relatively minor changes in loading may be influenced by a combination of creep, diffusion, and progressive failure effects. For example, Robertson et al. (2019) concluded that the sudden collapse of the Feijão Dam 1 near Brumadinho was attributable to a combination of creep and progressive failure effects in the hydraulically placed tailings following a loss of suction in unsaturated zones due to rainfall infiltration.

Plastic silts and clays exhibit viscous tendencies that can play a role in the static and dynamic performance of slopes and embankments. Most constitutive models do not directly incorporate viscous tendencies and instead rely on indirect allowances for their effects. Adjustments to shear strengths for earthquake loading rates are often selected from empirical correlations and the mesh-dependency of potential localizations is sometimes accounted for by implementing a length scale at a user-specified strain level (e.g., Kiernan and Montgomery 2018). In static analyses, viscous effects can help explain delays in deformations and instability relative to imposed loading, thereby being important for clarifying possible triggers for undrained failures such as observed at Feijão Dam 1 (Robertson et al. 2019). The direct incorporation of viscous tendencies in constitutive models can help regularize strain-softening simulations (reduce mesh dependency) and better account for the mechanical behaviors observed in the laboratory and field (e.g., Needleman 1988 and Niazi et al. 2013). Recently developed models such as MIT-SR (Yuan and Whittle 2020) and the BS-EVP framework (Shi and Hambleton 2019) directly incorporate viscoplasticity and provide an improved modeling of a broad range of strain rate-dependent behaviors. Nonetheless, there remains the need to have multiple models in software platforms that are commonly used in industry to help address model uncertainty when directly modeling viscoplasticity.

A viscoplastic bounding surface plasticity model (PM4SiltR) for representing strain rate-dependent shearing resistance in

Fig. 1. Strain rate effects on undrained monotonic loading response of clay: (*a*) undrained triaxial compression (TXC) stress–strain responses of undisturbed normally consolidated (NC) B-6 clay samples at three strain rates (Lefebvre and LeBouef 1987), and (*b*) peak undrained shear strength versus strain rate from 26 experimental programs compiled by Kulhawy and Mayne (1990).

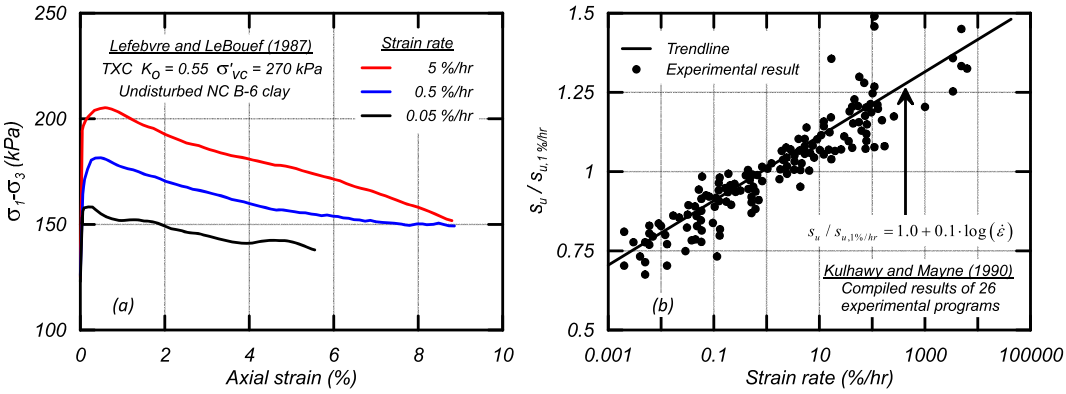

silts and clays in geotechnical static stability applications is presented. PM4SiltR builds upon the PM4Silt (Boulanger and Ziotopoulou 2019) model framework and is implemented as a dynamic link library (dll) for use in the finite difference program FLAC 8.1. PM4SiltR models strain rate-dependent shear strength, stress relaxation, and creep using a consistency approach combined with an internal strain rate and auto-decay process. The model does not include a cap and therefore is not suited to simulate consolidation under increasing overburden stress. PM4SiltR utilizes the same monotonic parameters as PM4Silt and introduces six new parameters to control the viscoplastic behaviors. The development of the model, the calibration process, and the influence of the viscoplastic parameters are described herein. The model is shown to capture a range of viscoplastic behaviors in a manner consistent with literature. Simulations of a hypothetical tailings dam constructed using the upstream method are performed to illustrate use of PM4SiltR at field scale. These simulations show PM4SiltR can model undrained creep and progressive failure leading to delayed slope instability after relatively minor changes in loading conditions at field scale.

Time-dependent clay behavior

Strain rate-dependent shear resistance

The undrained shear strength (s_u) of clays and plastic silts generally increases with the applied strain rate. Experimental results have shown that s_u increases approximately 5%–15% per log cycle of strain rate (Graham et al. 1983; Lefebvre and LeBouef 1987; Sheahan et al. 1996). The undrained triaxial compression (TXC) test results shown in Fig. 1*a* (Lefebvre and LeBouef 1987) for normally consolidated (NC) B-6 clay samples at axial strain rates of 0.05, 0.5, and 5%/h showed that increasing the strain rate increased the shear resistance over the range of imposed strains. Kulhawy and Mayne (1990) compiled data for 26 saturated clays and showed that peak s_u increased by an average of 10% per log cycle of strain rate (Fig. 1*b*). The data in Fig. 1*b* showed that the s_u at the smallest strain rates examined (i.e., 0.001–0.01%/h) was generally 70%–80% of the s_u at a standard laboratory strain rate of 1%/h (i.e., $s_{u,1\%/h}$). Kutter and Sathialingam (1992) and Ladd and DeGroot (2004) concluded that the change in s_u per log cycle of strain rate progressively increases with increasing strain rate. Diaz-Rodriguez et al. (2009) provided an overview of the effect of different soil characteristics and loading conditions on the magnitude of strain rate dependency.

Experimental results have indicated a potential lower limit of applied strain rate below which the s_u becomes independent of strain rate (Graham et al. 1983; Diaz-Rodriguez et al. 2009; Gylland et al. 2014). Other researchers have postulated that this lower limit exists, although experimental data do not clearly define the strain rate at which this occurs (Sheahan et al. 1996; Ladd and DeGroot 2004). Data from field vane tests at varying vane velocities supported a lower limit of strain rate dependency with a lower limit s_u of approximately 70% of the s_u at a reference rate (Peuchen and Mayne 2007).

The mechanisms underlying strain rate dependency of s_u have been attributed to changes in friction angle (or failure envelope), suppression of shear-induced pore pressure, or a combination of these two mechanisms. Differentiating between these mechanisms in experimental programs can be complicated by limitations in pore pressure measurements during rapid undrained shearing, wherein pore pressure measurements at the ends or middle of a specimen may not represent an average value for the entire specimen (e.g., Zergoun and Vaid 1994). TXC test data on compacted clay have suggested that the increased shear strength is due to suppression of shear-induced pore pressures at high strain rates (Mun et al. 2016). Triaxial tests for reconstituted London Clay showed that the shearing resistance had a strain rate dependency at low strains but a diminishing dependency with increasing post-peak strain levels, whereas tests for undisturbed London Clay showed strain rate dependency that persisted both pre- and post-peak (Sorenson et al. 2007). Sheahan et al. (1996) and Lefebvre and LeBouef (1987) suggested that the strain rate dependency in their experimental results may

Fig. 2. Triaxial creep tests by Lacerda (1976) on undisturbed normally consolidated (NC) San Francisco (SF) Bay Mud: (*a*) strain rate and (*b*) axial strain versus time.

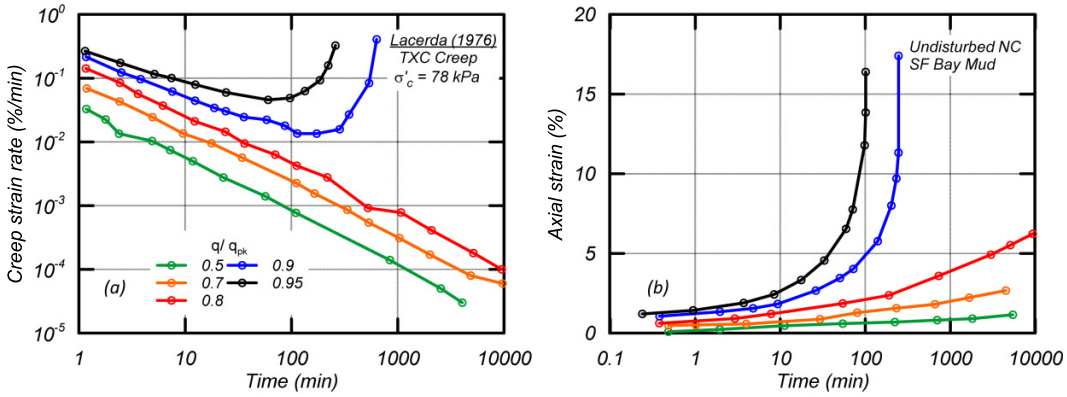

be due to a combination of the two mechanisms and that their effects may vary depending on the overconsolidation ratio (OCR) and other soil properties.

The residual shear resistance of clay and clay-slickensided surfaces in drained direct shear tests also exhibits strain rate dependency, as illustrated by the results in Skempton (1985) showing a small effect at the slowest strain rates (e.g., 2.5% per log cycle) but large effects at faster shearing rates (e.g., 100% gains at the highest strain rates). The strain rate dependency of residual shear resistance has been attributed to a combination of changes in residual friction angle and local changes in pore pressure during fast shearing (Skempton 1985). Laboratory and centrifuge model tests by others have reached similar conclusions (e.g., Meehan et al. 2008).

The undrained and drained stress–strain responses of saturated clay may reasonably be expected to have different strain rate dependencies at different points of loading (small strains, peak resistance, critical state, large strains, etc.) given that the underlying fundamental mechanisms for strain rate dependency may be different at each strain level and are likely to depend on the soil characteristics (mineralogy, structure, stress history, age, etc.). Fundamental processes underlying strain rate dependency of frictional shear resistance and dilatancy of granular materials (including clays) from the low strain rate (quasi-static) to high strain rate regimes are described by Santamarina and Shin (2009).

Creep

Clays subjected to sustained shear stresses continue to creep (deform) over time. Results for five undrained TXC creep tests at sustained stress levels equal to 50%, 70%, 80%, 90%, and 95% of the peak s_u (for the reference strain rate) on undisturbed San Francisco (SF) Bay Mud (Lacerda 1976) are shown in Fig. 2 in terms of creep strain rate (Fig. 2*a*) and strain (Fig. 2*b*) versus time. Higher sustained stress levels resulted in larger creep strain (Fig. 2*b*). Creep strain rate initially decreased in time (Fig. 2*a*) for all sustained stress levels. Samples loaded at stress levels below 80% of peak s_u deformed with a continually decreasing creep strain rate throughout the duration of the test indicating a stable condition. Creep strain rates for samples loaded at 90% and 95% of peak s_u initially decreased before rapidly increasing to an undrained creep rupture (sample collapse). Vaid et al. (1979) related the observance of a minimum strain rate during a creep test as a sign of an impending rupture. Vaid et al. (1979) and Sheahan (1995) suggested the existence of a yield strength below which creep rupture will not occur and deformations stabilize. Sheahan (1995) connected this behavior to the static yield surface introduced in elastic/viscoplastic (EVP) models. Lacerda (1976) found that the peak s_u strain rate dependency can be determined from creep parameters and that creep parameters can be used to predict the stress–strain curve in undrained shearing at low strain levels.

Stress relaxation

Clays held at a constant strain after loading to a defined stress level shed stress over time, a process known as stress relaxation. The rate of stress relaxation was linear with the logarithm of time for three different clays in laboratory testing (Lacerda 1976). Experimental studies have shown the potential existence of a lower limit on stress levels below which further stress relaxation will not occur (Silvestri et al. 1988) as shown in Fig. 3. Silvestri et al. (1988) indicated that the time for stress relaxation may differ depending on loading conditions that are supported by Lacerda's (1976) observation that the time at which relaxation initiated is dependent on the strain level prior to relaxation. Lacerda (1976) asserted that the rate of relaxation was independent of strain rate and strain prior to the relaxation stage. Lacerda (1976) also showed that the slope of the strength versus logarithm of strain rate (e.g., Fig. 1) was approximately equal to the slope of the stress relaxation curve (e.g., Fig. 2), indicating that creep parameters can be used to predict stress relaxation parameters.

1-D compression

The apparent preconsolidation pressure in 1-D consolidation testing depends on the applied consolidation strain rate. Behavior at significant OCRs does not appear to be rate dependent with recompression curves being largely inviscid regardless of the applied consolidation strain rate. This behavior is consistent with peak strength rate dependency less-

Fig. 3. Four triaxial compression (TXC) stress relaxation tests by Silvestri et al. (1988) on normally consolidated (NC) Louiseville clay at different deviator stress levels showing the relaxation of deviator stress in time.

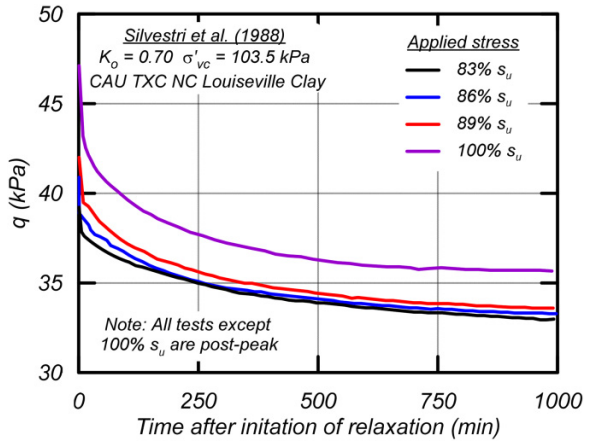

Fig. 4. Strain rate effects on the apparent preconsolidation pressure versus strain rate for a compilation of consolidation tests by Leroueil et al. (1983).

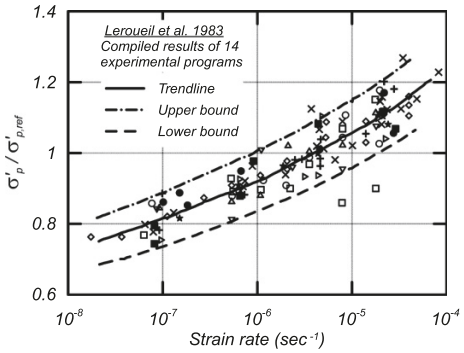

ening when the OCR is significant. Rate dependency resulted in a preconsolidation pressure and virgin compression line that were unique for each applied consolidation strain rate, referred to as isotaches. Rate dependency has been shown to become negligible at lower consolidation strain rates (Vaid et al. 1979). Compilations of data for various clays suggested that this lower limit tends to be approximately 70% of the preconsolidation pressure for a reference consolidation strain rate (Fig. 4; Leroueil et al. 1983; Watabe et al. 2012). The rate dependency of the preconsolidation pressure was shown to be approximately 5% per log cycle of applied consolidation strain rate near the reference strain rate (Leroueil 2006).

Rate-dependent constitutive models

Viscoplastic constitutive models have been developed using different viscoplasticity approaches combined with different constitutive frameworks. Recent examples include several built on the Modified Cam Clay framework (Yin et al. 2006, 2011, 2015; Rezania et al. 2016) and several that use a bounding surface plasticity framework (Martindale et al. 2012; Shi and Hambleton 2019; Kutter and Sathialingam 1992; Jiang et al. 2017).

Wang et al. (1997) examined three approaches to incorporating viscoplasticity in constitutive models: the overstress viscoplasticity approaches by Perzyna (1963) and Duvaut-Lions (1972) and a consistency viscoplasticity approach. Perzyna (1963) presented a constitutive framework that separated elastic and viscoplastic strains with a static yield condition; the stress difference between the current loading state and the static yield surface is termed the overstress, and this approach was termed EVP. A distinction was made between EVP and elastic–viscoplastic behavior which had viscous behavior in both the elastic and plastic regimes. The viscoplastic strain rate in the overstress approach of Perzyna (1963) is determined by the value of the yield function, whereas the viscoplastic strain rate in the approach of Duvaut and Lions (1972) is determined by the overstress. The consistency viscoplasticity approach introduced in Wang et al. (1997) instead incorporates viscoplasticity by introducing a rate-dependent yield surface defined as follows:

$$f(\sigma, \kappa, \dot{\kappa}) = 0$$

where σ is the stress tensor, κ is the equivalent plastic strain, and $\dot{k}$ is the equivalent plastic strain rate. A major difference between the consistency and overstress approaches is that the stress state cannot exist outside of the yield surface in the consistency approach, whereas the stress state can be outside the yield surface in the overstress approaches. The consistency approach also enables the yield function to grow and shrink not only due to hardening and softening, but also with increasing and decreasing strain rate. Wang et al. (1997) provided a derivation of how the consistency approach with its strain rate-dependent yield function can be incorporated in a finite element analysis and further provided a fully implicit stress-update algorithm that is not dependent on the viscoplastic strain rate (because that dependency is in the yield surface) unlike the overstress approaches.

Examples of viscoplastic constitutive models that use a consistency approach include the soil models by Wedage et al. (1998) and Martindale et al. (2012). Wedage et al. (1998) used the consistency approach to model strain rate effects on the residual shear strength of clay, with the effective friction angle being a function of the strain rate. Martindale et al. (2012) used a modified consistency approach which introduced strain rate dependency by shifting the critical state line (CSL) in e-log p′ space. In a consistency approach, the strain rate-dependent features of a constitutive model should evolve smoothly over time in response to step changes in the imposed strain rate, rather than shift instantaneously in response to such changes. Internal strain rate parameters and auto-decay processes, which can be related to the natural decay of strain-rate concept described in Singh and Mitchell (1968), have been introduced in models to regulate the time-dependent response of internal variables to variations in the imposed strain rate (e.g., Clarke and Hird 2012; Yuan and Whittle 2018, 2020).

Model development

The model formulation for PM4SiltR builds directly on the PM4Silt model by Boulanger and Ziotopoulou (2019). Modifications were made to represent viscous effects such as strain rate-dependent shear strength, creep, and stress relaxation. PM4SiltR is implemented as a dll in FLAC 8.1 (Itasca 2019) and is thus a plane strain model. Its implementation in the explicit finite difference framework of FLAC is identical to PM4Silt except that the model was formulated for use with the creep module instead of the dynamic module.

The base model PM4Silt is a critical state-based, stress ratio-controlled, bounding surface plasticity model that builds upon the PM4Sand constitutive model described by Boulanger and Ziotopoulou (2017) and Ziotopoulou and Boulanger (2016). PM4Silt was developed to represent clays and plastic silts in geotechnical earthquake engineering applications. PM4Silt has three required input parameters: (1) the critical state strength or strength ratio under earthquake loading rates ($s_{u,cs,eq}$ or $s_{u,cs,eq}/\sigma'_{vc}$, where σ'_{vc} is the vertical effective consolidation stress), (2) the shear modulus coefficient (G_o), and (3) the contraction rate parameter (h_{po}). The model has an additional 20 secondary parameters that receive either default values or can be modified to account for site-specific data. Further discussion of the parameters and the model itself can be found in Boulanger and Ziotopoulou (2019). PM4Silt does not include a cap and therefore is not suited to simulate consolidation under increasing overburden stress. PM4Silt does not simulate viscous effects and is unable to model stress changes or deformations in time due to stress relaxation or creep.

Viscoplasticity was added to the PM4Silt model using the previously described consistency approach (Wang et al. 1997; Martindale et al. 2012) with transient responses and stress relaxation controlled through an internal strain rate and autodecay process (Clarke and Hird 2012; Yuan and Whittle 2018, 2020). The consistency approach was applied to the bounding, dilatancy, and critical state surfaces of the model (in q-p′ space) to simulate the potential mechanism of a shifting the failure envelope (Lefebvre and LeBouef 1987; Sheahan et al. 1996) and to the CSL in e-ln(p′) space to simulate the potential mechanism of suppressing shear-induced pore pressure (Lefebvre and LeBouef 1987; Sheahan et al. 1996; Sorenson et al. 2007). The formulation of the model allows for the user to adjust the relative contributions of these two mechanisms in producing strain rate dependency. The consistency approach enables accounting for viscous effects by utilizing the formulation of the PM4Silt constitutive model without necessitating reformulation of the model around a viscoplastic strain rate and viscous material properties. Accordingly, the numerical implementation for PM4SiltR within the explicit finite difference framework of FLAC is identical to that for PM4Silt, with the details fully described in Boulanger and Ziotopoulou (2019).

Development of the strain rate-dependent features of the PM4SiltR model emphasized (1) obtaining reasonable approximations of the strain rate effects most important to static slope stability applications and (2) ease of calibration to empirical correlations or site-specific testing data. Strain rate dependency of s_u and undrained creep were given particular emphasis during model development. The calibration process was simplified by (1) using the consistency approach because it allowed use of constitutive equations that follow the form of common empirical relationships or trends, and (2) assuming that the mechanisms and parameters controlling strain rate dependency are active/constant across the full range of small to large strains.

Rate-dependent plasticity surfaces

The bounding, dilatancy, and critical state surfaces of the model were made strain rate dependent using a consistency approach. The model defines critical state using a critical state stress ratio (M) and a linear CSL in void ratio (e) versus natural logarithm of mean effective stress (ln p′) space where the slope is λ and intercept e_{1kPa} when p'=1 kPa. This can be expressed as follows:

$$(1) \qquad e_{cs} = e_{1kPa} - \lambda \ln\left(\frac{p'_{cs}}{1kPa}\right)$$

The p'_{cs} and M were made dependent on the internal strain rate ($\dot{\bar{\gamma}}$) as

$$(2) \qquad M = M_{ref}\left(1 + F_M \log\left(\frac{\dot{\bar{\gamma}}}{\dot{\gamma}_{ref}} + R_{\dot{\gamma},\min}\right)\right)$$

$$(3) \qquad p'_{cs} = p'_{cs,ref}\left(1 + F_p \log\left(\frac{\dot{\bar{\gamma}}}{\dot{\gamma}_{ref}} + R_{\dot{\gamma},\min}\right)\right)$$

where $\dot{\gamma}_{ref}$ = reference strain rate, $p'_{cs,ref} = p'_{cs}$ at the reference strain rate, $M_{ref} = M$ at the reference strain rate, F_M and F_p are rate parameters for M and p'_{cs}, respectively, and $R_{\dot{\gamma},\min}$ is the minimum normalized strain rate producing a viscid response. The strain rate dependence of p'_{cs}, which is not a model parameter, is implemented via the equivalent strain rate dependency of the CSL parameter e_{1kPa} as

$$(4) \qquad e_{1kPa} = e_{1kPa,ref} - \lambda \cdot \ln\left(1 + F_p \log\left(\frac{\dot{\bar{\gamma}}}{\dot{\gamma}_{ref}} + R_{\dot{\gamma},\min}\right)\right)$$

where $e_{1kPa,\,ref} = e_{1kPa}$ at the reference strain rate. F_M and F_p can be adjusted independently of each other to obtain the desired shear strength strain-rate dependency of the soil based on the user's interpretation of each mechanism's role. Setting F_M and F_P equal to each other may provide a reasonable compromise for most calibrations, recognizing that both mechanisms likely contribute to observed strain rate dependencies in clays and plastic silts. The above equations utilize the base ten logarithm to be consistent with common experimental and empirical forms. $R_{\dot{\gamma},\min}$ determines the strain rate below which the behavior transitions from viscoplastic to inviscid, with the default value of 0.001 corresponding to a strain rate three orders of magnitude below the reference rate. The default $R_{\dot{\gamma},\min}$ value was selected for consistency with the experimental data summarized in Fig. 1*b* (Kulhawy and Mayne 1990) and corresponds to the strain rates at which minimum shear strenths equal to 70%–75% of the peak undrained strength at the reference strain rate were obtained.

Fig. 5. Rate dependent: (*a*) critical state lines in e-log(p') space, and (*b*) bounding surfaces in q-p' space at different strain rate ratios (SRRs).

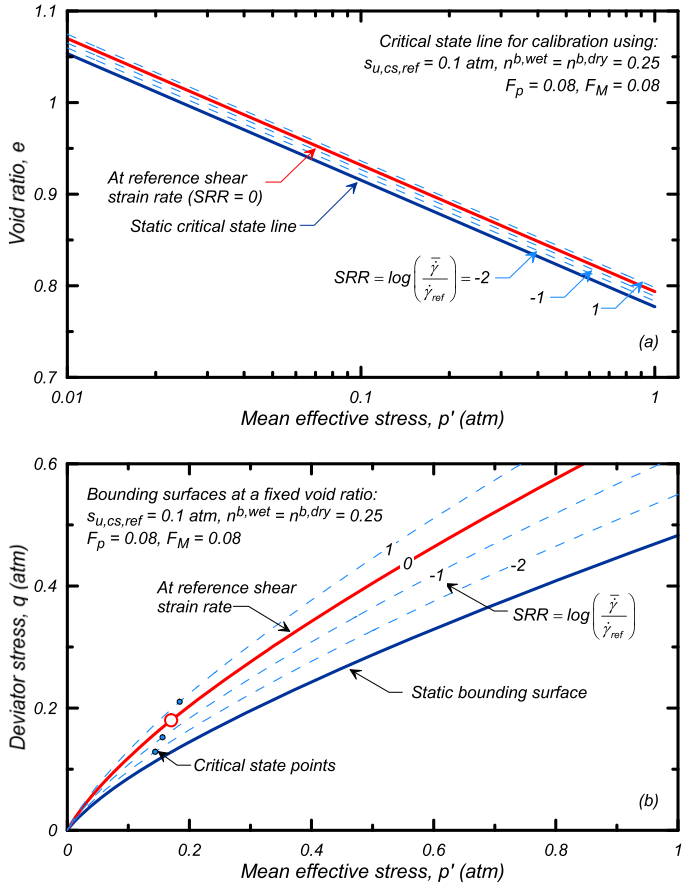

The rate dependency of the CSL is illustrated in Fig. 5*a* for an example set of calibration parameters (referred to as Calibration B and described in a later section). Strain rates are expressed as strain rate ratios (SRRs) defined as:

$$SRR = \log\left(\frac{\dot{\bar{\gamma}}}{\dot{\gamma}_{ref}}\right) \quad (5)$$

The reference CSL (at SRR = 0) is equivalent to the CSL without viscoplasticity. An increasing SRR shifts the CSL to the right in e-ln(p') space by a magnitude controlled by the F_p parameter. A rightward shift in the CSL increases p' at critical state and thus decreases the state parameter. A decreasing SRR shifts the CSL to the left, with the leftward limit being the static CSL for a zero strain rate condition. CSLs for SRRs less than log($R_{\dot{\gamma},\min}$) are approximately equal to the static CSL. The effect of SRR on the CSL position is independent of the loading direction or current stress state.

The rate dependency of the bounding surface is illustrated in Fig. 5*b*. The bounding surface for looseness of critical state conditions is dependent on M and the state parameter ξ as,

$$M_b = M \cdot \exp\left(-n^{b,wet}\xi\right) \quad (6)$$

where $n^{b,wet}$ is a positive number so that M_b is smaller than M on the wet side of critical state. The bounding surface for dry of critical state conditions has a different functional

Fig. 6. Variation in peak shear strength versus strain rate ratio (SRR) for single element simulations of direct simple shear (DSS, blue), plane strain compression (PSC, red), and plane strain extension (PSE, green).

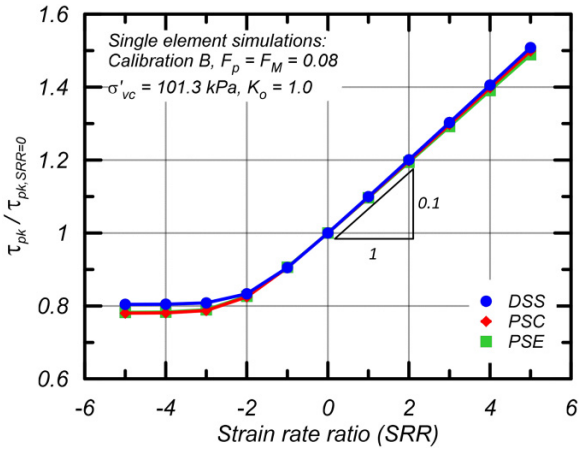

form (Boulanger and Ziotopoulou 2019), but the key feature is that M_b is greater than M on the dry side of critical state. Rate-dependent bounding surfaces for different SRRs are illustrated in Fig. 5*b* for undrained loading (fixed void ratio) of a soil with an $s_{u,cs,ref} = 0.2$ atm and $F_p = F_M = 0.08$. Increasing the SRR shifts the bounding surface upwards in q-p' space due to the rightward shift in the CSL (Fig. 5*a*, eq. 4) and increase in M (eq. 2), as illustrated by the relative movements of the critical state points marked on the bounding surfaces for each SRR in Fig. 5*b*.

The static bounding surface ($M_{b,static}$) separating viscoplastic from inviscid behaviors is the bounding surface for a zero strain rate loading condition. The location of the static bounding surface is controlled by $R_{\dot{\gamma},\min}$, F_p, and F_M. The CSL and static bounding surface shown in Figs. 5*a* and 5*b*, respectively, are for simulations with $R_{\dot{\gamma},\min} = 0.001$ and $F_p = F_M = 0.08$. M and p'_{cs} for static loading conditions are

$$p'_{cs,static} = p'_{cs,ref}\left(1 - \log\left(R_{\dot{\gamma},\min}\right)F_p\right) \quad (7)$$

$$M_{static} = M_{ref}\left(1 - \log\left(R_{\dot{\gamma},\min}\right)F_M\right) \quad (8)$$

For the parameters used to generate Fig. 5 (i.e., Calibration B), the result is that $M_{static} = 0.76M_{ref}$ and $p'_{cs,static} = 0.76p'_{cs,ref}$.

The rate dependency of peak shear strength (τ_{pk} or s_u) is illustrated in Fig. 6 showing $\tau_{pk}/\tau_{pk,SRR=0}$ versus SRR for single element simulations of undrained loading in direct simple shear (DSS), plane strain compression (PSC), and plane strain extension (PSE). These results were similarly based on Calibration B. Over a range of SRRs from −2 to 5, the trends were approximately linear for all loading conditions with a 10% change in s_u per log cycle of strain rate. At SRRs < −2, the change in s_u with strain rate flattened with the lower bound corresponding to the static (inviscid) bounding surface. The rate dependency and lower bound on s_u are the same for PSC and PSE, as expected, because the initial stress state was isotropic (i.e., $K_o = 1.0$) and the model is not depen-

dent on the Lode angle. The lower bound on s_u at SRRs < −2 for DSS differs slightly from that for PSC and PSE because of the slight changes in K_o that occur during DSS loading. DSS, PSC, and PSE simulations with different initial K_o values will produce a degree of s_u anisotropy that depends on the material calibration, and thus may also produce some differences in the lower bound $s_u/s_{u,SRR=0}$ ratios and strain rate dependency (percentage change per log cycle of strain rate) for SRR of −2 to 5. Note that the rate dependency at SRR > 5 (beyond the range of interest and outside the range shown in Fig. 6) will plateau because the current numerical implementation limits the bounding stress ratio to less than 1.7 times the reference critical state stress ratio (this corresponds to limiting the mobilized friction angle to about twice the reference critical state value).

Internal strain rate

Transient responses to changes in the external strain rate are controlled through updating the internal strain rate ($\bar{\dot{\gamma}}$) with the internal strain rate parameter θ_{ref}. At the end of each time step, the internal strain rate is updated based on the instantaneous external strain rate ($\dot{\gamma}$) and θ_{ref} as

$$\bar{\dot{\gamma}}_{i+1} = \bar{\dot{\gamma}}_i \theta + \dot{\gamma}_{i+1}(1-\theta) \quad (9)$$

$$\theta = \theta_{ref} + (1-\theta_{ref})B \quad with \quad 0 \le \theta \le 0.99 \quad (10)$$

where B is a time smoothing factor based on the current time step size and a reference time step size,

$$B = 1 - \frac{\Delta t}{\Delta t_{ref}} \quad (11)$$

$$\Delta t_{ref} = \frac{m\, p'}{G\, \dot{\gamma}_{ref}} \quad (12)$$

where m = size of the elastic zone, p' = current mean effective stress, and G = shear modulus. Larger θ_{ref} values result in a slower evolution of the internal strain rate toward the applied strain rate when the applied strain rate changes. θ_{ref} = 0.5 resulted in the internal strain rate adjusting to a step change in external strain rate over approximately 0.25% shear strain while θ_{ref} = 0.95 updated over approximately 2% shear strain, as illustrated by the example in Fig. 7. A larger θ_{ref} value increases the number of steps required for the internal strain rate to converge toward the external strain rate after a step increase in the external strain rate. The time smoothing factor (B) increases θ as the time step is reduced, increasing the number of steps needed for the internal strain rate to adjust to changes in external strain rate. This ensures that the evolution of internal strain rate occurs over a reasonable magnitude of strain. The reverse is true as the time step is increased, except θ goes to zero and the number of steps to adopt a new strain rate is reduced, while the strain increment required for evolution of internal strain rate remains approximately the same.

Relaxation and creep

Stress relaxation is imposed when the current stress ratio (η) is above the bounding surface, with the rate of relaxation proportional to the difference between η and M_b. A stress relaxation process is required for this situation because, when the imposed strain rate drops to zero and the operational bounding surface is above the static bounding surface, there is no other mechanism for the stresses to relax toward the static bounding surface. The relaxation process ceases when the current stress state has dropped to the static bounding surface, or when a strain rate is imposed and the bounding surface increases either to or above the current stress state. The deviator stress ratio tensor ($\mathbf{r}$) and back-stress ratio tensor ($\boldsymbol{\alpha}$) are relaxed as follows:

$$\mathbf{r}_{i+1} = \mathbf{r}_i C_r \quad (13)$$

$$\boldsymbol{\alpha}_{i+1} = \boldsymbol{\alpha}_i C_r \quad (14)$$

where the stress relaxation parameter C_r is computed as

$$\beta = \beta_{ref} + (1-\beta_{ref})B \quad (15)$$
$$0 \le \beta \le 1$$

$$C_r = \frac{M_b}{\eta} + \frac{\eta - M_b}{\eta}\beta \quad (16)$$
$$C_r \le 1$$

The auto-decay parameter β_{ref} corresponds to the fraction of η—M_b that remains after relaxation in a time increment equal to Δt_{ref}. This means that a β_{ref} = 0.99 corresponds to 1% of η—M_b relaxed every Δt_{ref} increment of time. β_{ref} = 1.0 eliminates stress relaxation, while β_{ref} = 0.0 results in instantaneous relaxation. The auto-decay parameter β is adjusted from the input β_{ref} with the time smoothing factor B to reduce the dependency on the time step size as done in the internal strain rate calculation. The parameter C_r reduces the current stress ratio toward M_b by an amount proportional to the difference between η and M_b, resulting in exponential relaxation. Stress relaxation ceases when η is reduced to or below the bounding surface.

The stress relaxation mechanism is illustrated in q−p′ space and time–stress ratio space in Fig. 8. The simulation in

Fig. 7. Internal strain rate evolution with varying internal strain rate parameter (θ_{ref}).

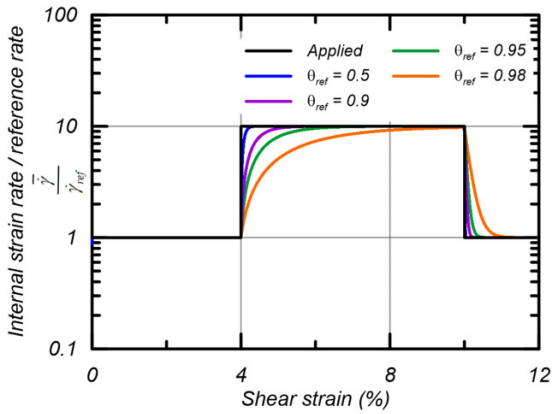

Fig. 8. Stress relaxation mechanism shown as (*a*) stress path in q-p′ space and (*b*) stress ratio reduction in stress ratio–time space for an undrained direct simple shear (DSS) simulation.

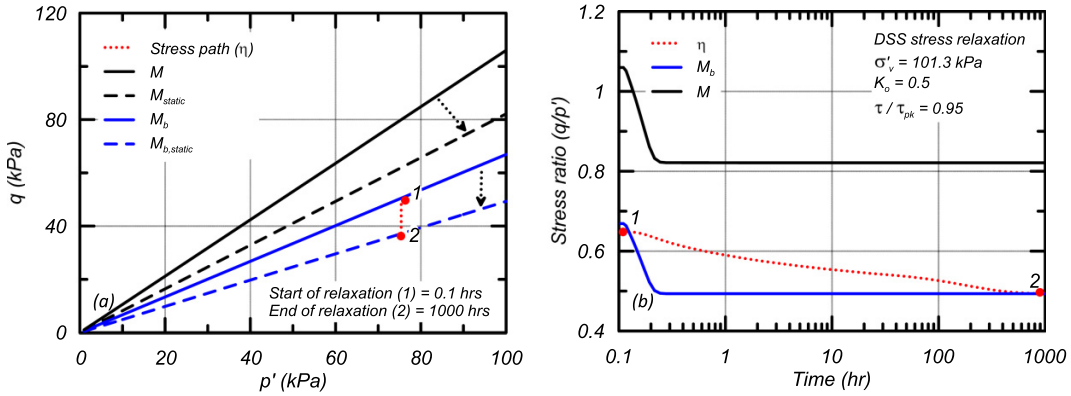

Table 1. Input parameters for PM4SiltR model.

Parameter	Description	Effect	Default value
F_p	Rate parameter for p'_{cs}	Sets the rate dependency of the critical state line	0.0
F_M	Rate parameter for M	Sets the rate dependency of the M line	0.0
$\dot{\gamma}_{ref}$	Reference shear strain rate (per second)	Sets the reference rate for calculation of the strain rate ratio	5% per hour
$R_{\dot{\gamma},\min}$	Minimum normalized strain rate	Sets the placement of the static bounding surface	0.001
θ_{ref}	Internal strain rate parameter	Controls the transient response to changes in external strain rate	0.5
β_{ref}	Auto-decay parameter	Controls the rate of stress relaxation	0.999

Fig. 8 shows an element that underwent DSS loading to point A, after which the strain rate was set to zero (i.e., displacements fixed). Upon cessation of straining, the bounding surface evolved from M_b (blue solid line) to $M_{b,static}$ (blue dashed line) over approximately 0.3 h (Fig. 8*b*); the length of time is dictated by the evolution of the internal strain rate. The lowering of the bounding surface with a reducing internal strain rate resulted in η being larger than M_b at approximately 0.12 h, which induced the stress relaxation mechanism. The relaxation in stress ratio can be seen in the red line as a steady reduction until the stress ratio reached the static bounding surface at approximately 1000 h. This correlated to the reduction in deviator stress seen in the stress path in q−p′ space. For fixed-stress boundary conditions (as opposed to fixed displacement), this stress relaxation mechanism instead contributes to the accumulation of strain (i.e., creep) at a strain rate necessary to resist the imposed fixed-stress boundary condition.

Strain rate parameters

Six parameters control the viscous response of the model as shown in Table 1. F_p and F_M control the strain rate dependency of the CSL and M, respectively. $\dot{\gamma}_{ref}$ sets the reference rate for the base calibration. Placement of the static bounding surface and the corresponding distinction between inviscid and viscoplastic behavior is determined by $R_{\dot{\gamma},\min}$, F_p, and F_M. The transient response to external variations in strain rate is controlled by θ_{ref} while the rate of stress relaxation is controlled by β_{ref}.

Calibration procedure

PM4SiltR is controlled by 24 parameters; out of those, 12 are the parameters that control the monotonic response of PM4Silt, 6 control the viscous portion of the response, and 6 control cyclic aspects of the response. The preceding section focused on the viscous portions of the model; readers are referred to Boulanger and Ziotopoulou (2019) for full details of the PM4Silt model. The procedure outlined below can be used to calibrate the model with differing levels of site-specific soil information. Further information on calibration for rate effects can be found in Boulanger et al. (2022) and Oathes (2022).

1) Select values for the critical state undrained shear strength ($s_{u,cs,ref}$) or undrained shear strength ratio ($s_{u,cs,ref}/\sigma'_{vc}$), and the corresponding reference shear strain rate ($\dot{\gamma}_{ref}$).
2) Select the shear modulus coefficient (G_o) and shear modulus exponent (n_g) to match the estimated small-strain shear modulus (G_{max}) and its variation with depth.
3) Select values for any secondary parameters that can be informed by soil-specific test data, such as e_o, λ, and ϕ'_{cv}.
4) Simulate undrained monotonic loading (DSS, PSC, or PSE) at the reference strain rate and iteratively adjust $n_{b,wet}$ to obtain the desired peak strength and compare to laboratory test data. Iteratively adjust the plastic modulus parameter (h_o) and contraction rate parameter (h_{po}) to adjust the stress–strain response as desired.

Table 2. PM4SiltR calibrations input parameters.

	Calibration	A	B	C	D	E	F	G
PM4Silt	$s_{u,cs,ref}/\sigma'_{vc}$	0.09	–	–	–	–	–	–
	G_o	500	–	–	–	–	–	–
	h_{po}	250	–	–	–	–	–	–
	$n^{b,wet} = n^{b,dry}$	0.25	–	–	–	–	–	–
	h_o	0.1	–	–	–	–	–	–
PM4SiltR	F_p	0.0	0.08	0.08	0.08	0.05	0.1	0.0
	F_M	0.0	0.08	0.08	0.08	0.05	0.0	0.1
	$R_{\dot{\gamma},min}$	0.0	0.01	0.001	0.1	0.001	0.001	0.001

Fig. 9. Peak shear strength rate dependency expressed as normalized peak shear strength versus strain rate ratio (SRR) with varying: (*a*) $R_{\dot{\gamma},min}$ and (*b*) magnitudes of F_p and F_M.

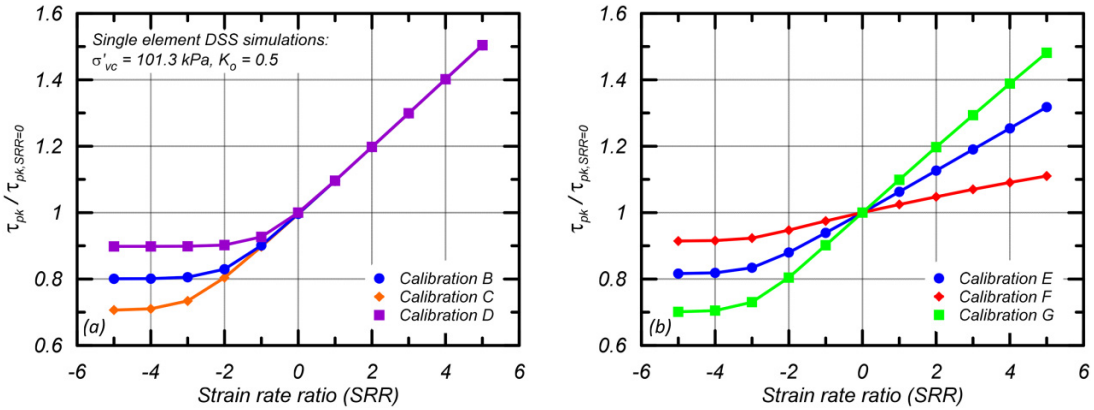

5) Simulate undrained monotonic loading for a range of strain rates and iteratively adjust F_p, F_M, and $R_{\dot{\gamma},min}$ to obtain the desired variation in peak s_u with strain rate. Rate dependency for critical state strength may vary from that of peak strength and thus it should be evaluated separately for cases where it is important to the system response.
6) Simulate undrained creep rupture and compare the results to any site-specific laboratory test data or empirical correlations. The time to rupture for a given stress level depends on several factors including: h_{po} (rate of strain softening), the F_p and F_M rate parameters, and the auto-decay parameter (β_{ref}).
7) Repeat steps 4–6 as needed.

The above procedure can utilize site-specific laboratory test data when available or can rely solely on empirical correlations (e.g., Figs. 1 and 2). Steps 1–4 largely follow the PM4Silt calibration procedure while steps 5–6 focus on the viscous behavior. The calibration process can be dependent on the types of analysis performed at the system level such that it is important to make choices during the calibration procedure that consider the behaviors of interest (e.g., the calibration for a drained versus undrained loading problem may differ). Model response should be examined for all loading paths that are expected to be important to the system-level response.

Constitutive responses

Single element simulations were performed to illustrate the constitutive response of PM4SiltR under a variety of loading conditions using different calibrations (Table 2). All calibrations had the same PM4Silt monotonic parameters that controlled the inviscid portion of the response. The inviscid response was calibrated to emulate a hypothetical, moderately sensitive, plastic clay or tailing material with common engineering properties. Calibration (A) was inviscid and illustrated the response in the absence of viscoplasticity. Calibration B was the baseline calibration and had a rate dependency of 10% per log cycle. Calibrations C–G varied the six parameters controlling viscous responses. All parameters not indicated in Table 2 maintained their default values. The introduced viscous parameters allow for flexibility in the magnitude and function of the imposed viscous effects.

Undrained shear at different strain rates

The variation of $\tau_{pk}/\tau_{pk,SRR=0}$ versus SRR is shown in Fig. 9 for the six calibrations and undrained DSS loading with $\sigma'_{vc} = 101.3$ kPa, $K_0 = 0.5$, and SRRs ranging from −5 to 5. Responses for Calibrations B, C, and D, all used $F_p = F_M = 0.08$, are compared in Fig. 9*a* to illustrate the effect of $R_{\dot{\gamma},min}$. These three calibrations had the same 10% change in $\tau_{pk}/\tau_{pk,SRR=0}$ per log cycle of strain rate for SRR > −1, but had different lower limits on $\tau_{pk}/\tau_{pk,SRR=0}$. Calibrations B ($R_{\dot{\gamma},min} = 10^{-2}$), C ($R_{\dot{\gamma},min} = 10^{-3}$), and D ($R_{\dot{\gamma},min} = 10^{-1}$) transitioned from

Fig. 10. Influence of strain rate on the stress–strain response in undrained direct simple shear (DSS) loading: (*a*) Calibrations A, E, F, and G with strain rate ratio (SRR) = 2, and (*b*) Calibration B with varying SRRs.

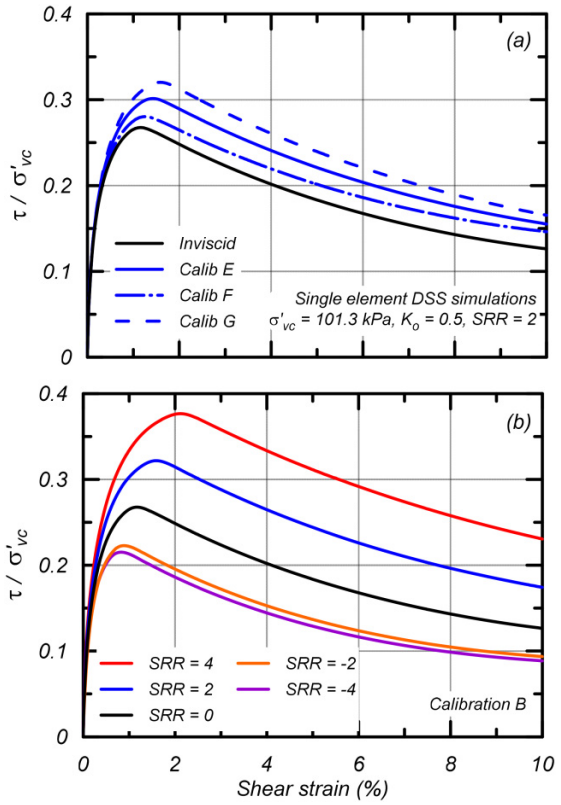

viscoplastic to inviscid at SRRs of approximately − 2, −3, and − 1, respectively, and had lower limits on $\tau_{pk}/\tau_{pk,SRR=0}$ of 0.8, 0.7, and 0.9, respectively (Fig. 9*a*). These results illustrated how $R_{\dot{\gamma},min}$ can be used to adjust the lower limit on $\tau_{pk}/\tau_{pk,SRR=0}$ (i.e., static undrained strength) after the values of F_p and F_M have been selected. Calibrations E, F, and G, all used $R_{\dot{\gamma},min} = 0.001$, are compared in Fig. 9*b* to illustrate the effect of F_p and F_M. Calibration F ($F_p = 0.1$, $F_M = 0.0$) had a strength increase of 2.5% per log cycle, while Calibration G ($F_p = 0.0$, $F_M = 0.1$) had a strength increase of 10% per log cycle as seen in Fig. 9*b*, illustrating how the peak s_u was more strongly influenced by F_M than F_p. Calibration E ($F_p = F_M = 0.05$) had an intermediate strength increase of 6.0% per log cycle (Fig. 9*b*). The lower limits on $\tau_{pk}/\tau_{pk,SRR=0}$ of 0.81, 0.92, and 0.70 for Calibrations E, F, and G, respectively, were directly related to their respective % changes in strength per log cycle of strain rate because all three used the same $R_{\dot{\gamma},min} = 0.001$.

The stress–strain response at different SRRs is influenced by F_p, F_M, and $R_{\dot{\gamma},min}$. Stress–strain responses in undrained DSS loading are shown for Calibrations A (inviscid case), E, F, and G at an SRR = 2 in Fig 10*a*. The shear strain at peak shear stress ($\gamma_{\tau,pk}$) increased with increasing peak strength, with $\gamma_{\tau,pk}$ increasing from 1.2% for the inviscid Calibration A to 1.4% to 1.6% for Calibrations E, F, and G. The simulations in Fig. 10*a* showed that including rate effects in Calibrations E, F, and G produced $\gamma_{\tau,pk}$ that were 15%–35% greater than the

Fig. 11. Direct simple shear (DSS) undrained creep simulations of Calibration B with varying sustained stress levels in shear strain versus time space.

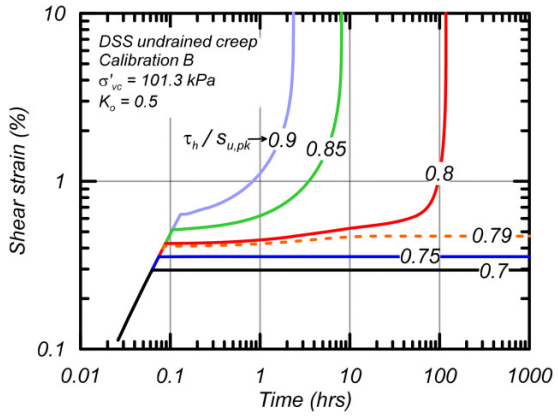

$\gamma_{\tau,pk}$ for the inviscid Calibration A. Stress–strain responses for baseline Calibration B are shown for undrained DSS simulations loaded at SRRs = −4, −2, 0, 2, and 4 in Fig. 10*b*. The peak shear strength increased approximately 10% per log cycle of loading rate at SRR > −2, consistent with the summary of these results in Fig. 9*a*. The $\gamma_{\tau,pk}$ increased by about 20% per log cycle of loading rate (e.g., from $\gamma_{\tau,pk} = 1.15\%$ at SRR = 0 to $\gamma_{\tau,pk} = 1.6\%$ at SRR = 2) over the same range of SRR values. The shear strength ratio reached its lower (inviscid) limit of about 0.21 when the SRR was less than −2. In addition, the effect of strain rate on $\tau_{pk}/\tau_{pk,SRR=0}$ is independent of σ'_{vc} for the same specified $s_{u,cs,ref}/\sigma'_{vc}$, but will vary with σ'_{vc} for the same specified $s_{u,cs}$ (i.e., with changing $s_{u,cs,ref}/\sigma'_{vc}$).

Undrained creep under sustained stress

The undrained creep response under DSS shearing for Calibration B with $\sigma'_{vc} = 101.3$ kPa and $K_0 = 0.5$ is shown for five loading conditions in Fig. 11. For these five simulations, the horizontal shear stress (τ_h) was increased to 70, 75, 80, 85, or 90% of $s_{u,pk,ref}$, after which the shear stress was held constant. Undrained creep rupture occurred for shear stresses above approximately 80% of $s_{u,pk,ref}$, whereas stable conditions developed for shear stresses below approximately 75% of $s_{u,pk,ref}$. The time to creep rupture reduced from approximately 118 h at $\tau_h/s_{u,pk,ref} = 0.8$–2.3 h for $\tau_h/s_{u,pk,ref} = 0.9$. For $\tau_h/s_{u,pk,ref} = 0.7$ and 0.75, the stress ratio was below the static yield surface and thus the element exhibited no creep. For $\tau_h/s_{u,pk,ref} \geq 0.8$, the stress ratio was significantly above the static yield surface and thus the element began developing creep strains. These creep strains increased K_0 but produced large reductions in p' such that the stress ratio remained above the static yield surface, which resulted in accelerating creep rates over time and eventually led to rupture. The occurrence of creep strains did not indicate an imminent creep rupture as seen for $\tau_h/s_{u,pk,ref} = 0.79$, where creep strains began to accumulate before stabilizing in time. In this condition, the stress ratio was slightly above the static yield surface and thus the element began to develop creep shear strains. The creep strains led to an increase in K_0 and slight reduction in p'; the stress

Fig. 12. Variation in applied strain rate (*a*) and stress–strain response (*b*) in undrained direct simple shear (DSS) loading.

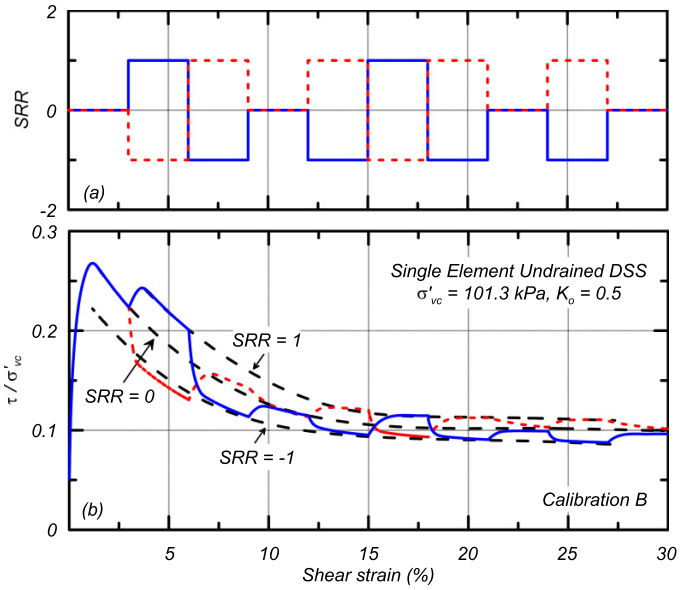

ratio eventually stabilized on the static bounding surface and creep deformations ceased. Sustained shear stresses near the static bounding surface stabilized or ruptured depending on the viscous properties, the sensitivity of material, and the rate of strain softening.

Undrained shear with step changes in strain rate

Stress–strain responses for undrained DSS loading with $\sigma'_{vc} = 101.3$ kPa and $K_0 = 0.5$ with step changes in strain rate (Fig 12*a*) are shown in Fig. 12*b* for Calibration B. Step-changed loading comprised 10 intervals of 3% shear strain with constant SRRs of −1, 0, and 1 (a range of two orders of magnitude); two sets of simulations are shown where the only difference was the order of applied rate changes. Following a step change in strain rate, the stress–strain response transitioned toward a shear resistance consistent with the newly imposed SRR. The transition in shearing resistance following a step change in strain rate takes about 0.25%–1.0% shear strain to fully develop depending on the magnitude of the change in strain rate, the strain level, and the model parameters. Dashed lines in Fig. 12 indicate an estimated fit of the intervals at unique SRRs. The steps did not directly fall onto the same line due to: (1) differences in internal strain rate evolution, (2) differences in the accumulation of plastic strain and the associated modulus reduction, and (3) the rate of post-peak strength loss. At larger strains (corresponding to lower shear resistances), the intervals corresponded more directly to the fit line because the magnitude of strength change per log cycle was smaller, which led to smaller differences in the evolution of the plasticity surfaces. Pre-peak stress–strain responses are unchanged with changing strain rate until close to mobilization of peak strength (Fig. 10) as the evolving plasticity surfaces do not influence the initial stiffness of the calibration. Figure 12 shows an evolution in the stress–strain response with changing strain rate that is consistent with observed stress–strain evolution for experimental results presented by Graham et al. (1983) for Winnipeg and Belfast clays subjected to similar strain-rate transitions.

Field scale response of a hypothetical tailings embankment

The response of a hypothetical tailings embankment to wetting events was modeled using the finite difference program FLAC 8.1 (Itasca 2019). The tailings embankment of upstream construction was 50 m tall, had a 4:1 horizontal to vertical slope, and was underlain by a 20 m thick foundation layer (Fig. 13). Elements in the finite difference mesh were 0.5 m tall by 1.0 m wide except in areas near the dikes and toe where the mesh was adjusted to accommodate the more complex geometry. The water table was at the tailings surface starting at a distance $\Delta X_{pool} = 210$ m from the head of the slope. Capillary rise was 6 m in the tailings and 1 m in the dikes. The hydraulic conductivity for the tailings and foundation were equal, while the conductivity for the dikes was 100 times larger. The horizontal conductivity was 10 times the vertical conductivity in all materials.

The tailings and foundation were modeled using PM4SiltR. The tailings were assumed to have uniform engineering characteristics represented by Calibration B or C. The peak undrained shear strength in DSS loading at standard laboratory strain rates ($s_{u,pk,ref}/\sigma'_{vc}$) was 0.27 and the critical state strength ($s_{u,cs,ref}/\sigma'_{vc}$) was 0.09, resulting in a sensitivity (S_t) of 3.0. The shear wave velocity at a confining pressure of 1 atm (101.3 kPa) was 145 m/s. An initial void ratio of 0.95 and a dry unit weight of 13.6 kN/m^3 were assumed. Calibrations B and C produced a strain-rate dependence in $s_{u,pk,ref}$ of 10% per log cycle of strain rate, with the lower (inviscid) limit on $s_{u,pk}$ being about 80% of $s_{u,pk,ref}$ for Calibration B and about 70% of $s_{u,pk,ref}$ for Calibration C (Fig. 6). The foundation layer was modeled using the same parameters as for the tailings except with $s_{u,cs,ref}/\sigma'_{vc} = 0.50$; this change produced a peak strength of $s_{u,pk,ref}/\sigma'_{vc} = 0.5$ with no post-peak strain softening (i.e., $S_t = 1.0$).

The dikes were modeled as medium-dense silty sand using PM4Sand. The input parameters were an apparent relative density $D_R = 55\%$, shear modulus coefficient $G_o = 677$, and contraction rate parameter $h_{po} = 0.4$; all other input parameters retained their default values. This calibration produced drained peak friction angles of 33–38 degrees in the dike depending on the loading path and effective confining stress.

Steady state seepage and initial static equilibrium conditions were established in a sequence of analysis steps as follows. Seepage and equilibrium conditions were first established using Mohr–Coulomb material models, after which the materials were switched to PM4SiltR with inviscid parameters (Calibration A) and PM4Sand, and equilibrium conditions solved for again. The viscous parameters for PM4SiltR were then activated (i.e., F_p, F_M, and $R_{\dot{\gamma},min}$ values for Calibration B or C) and a creep analysis initiated with

Fig. 13. Tailings impoundment geometry with the phreatic surface and saturation surfaces from the steady seepage analysis case for $\Delta x_{pool} = 210$ m.

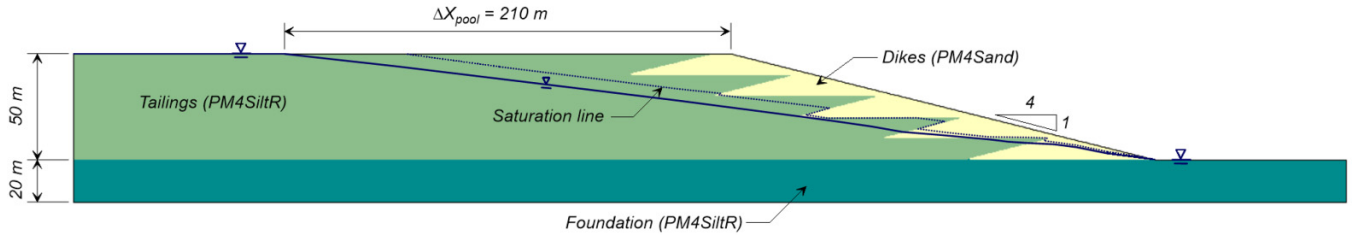

Fig. 14. Horizontal displacement at mid-slope versus time after start of creep analysis for Calibrations B and C with different wetting events.

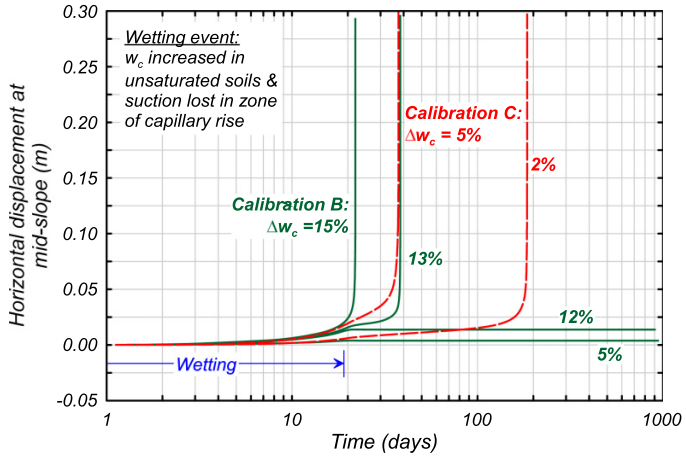

the tailings, foundation, and dikes fully drained. The creep analysis ended when creep deformations had ceased, corresponding to a long-term fully consolidated condition with all stress states either within or on the soil's static yield surface. In practice, the initialization of the model can have a significant impact on the results and it is important that the initial conditions of the model approximate the expected field conditions. The analyses shown herein are generally applicable for a range of initialization methods and provide an example of potential system level uses of the constitutive model.

The embankment was then subjected to a wetting event with undrained conditions in the saturated tailings and foundation layers and drained conditions in the sand dikes. A wetting event comprised increasing the water content (Δw_c) in the tailings and dike soils above those already saturated by capillary rise (dashed line in Fig. 13), while simultaneously eliminating the suction (negative pore pressures) in the soils saturated by capillary rise. The wetting event was ramped to the final loading condition over a period of approximately 18 days. Horizontal displacement of the embankment face at mid slope is plotted versus time since the start of the wetting event in Fig. 14 for analyses using Calibration B with imposed Δw_c of 5%, 12%, 13%, and 15% and Calibration C with imposed Δw_c of 2% and 5%. For the analyses using Calibration B, wetting events with $\Delta w_c \leq 12\%$ caused less than 15 mm of horizontal displacement at the embankment face, with most of the deformation occurring as the wetting load was imposed. The analyses using Calibration B with $\Delta w_c = 13\%$ and 15% developed slope instability in 23 days and 7 days, respectively, after the end of the wetting event. For both of these unstable cases, face displacements remained less than about 50 mm until a day before the slope became unstable. For the analyses using Calibration C, the wetting events with $\Delta w_c = 2\%$ and 5% developed instability in 168 and 20 days, respectively, after the end of the wetting event, with face displacements similarly remaining less than about 50 mm until a few days before the slope became unstable. The analyses using Calibration C ($R_{\dot{\gamma},\min} = 10^{-3}$) developed instability under much smaller wetting loads ($\Delta w_c = 2\%$ versus 13%) compared to Calibration B ($R_{\dot{\gamma},\min} = 10^{-2}$), taking an order of magnitude greater time to rupture after loading (168 days versus 23 days). These differences in responses were attributed to the order-of-magnitude smaller $R_{\dot{\gamma},\min}$ in Calibration C producing a 9% smaller static undrained shear strength at an order-of-magnitude smaller strain rates, such that undrained rupture at this lower strength required an order of magnitude more time to develop.

Wetting events that led to slope instability triggered progressive failure in the strain-softening tailings. Failure (post-peak softening) initiated in the tailings just above the foundation tailing interface around mid-slope of the embankment (the initially highest stressed zone) for all wetting events, leading to slope instability. The failure progression is illustrated in Fig. 15 showing shear strain contours for the simulation using Calibration C with a $\Delta w_c = 2\%$ at different times and hence different mid-slope horizontal displacements. Mid-slope displacement was 5 mm at 18 days in Fig. 14 (i.e., end of wetting) gradually increasing to 15 mm at 100 days, 25 mm at 158 days, 50 mm at 181 days, and 75 mm at 184 days, followed by the rapid progression of rupture strains and slope instability in less than 24 h (185 days). Zones of strain-softening, which corresponded approximately to the shear strain contours exceeding 1%–2% in Fig. 15, developed in localized shear bands such that global displacements remained relatively small even as the shear strains in these localization zones became relatively large. The zone of strain softening progressively grew in time, eventually developing along the full length of the eventual failure surface.

The progressive nature of the failure and the associated shedding of shear stress from softening elements explains

Fig. 15. Contours of shear strain at different times using Calibration C with $\Delta w_c = 2\%$.

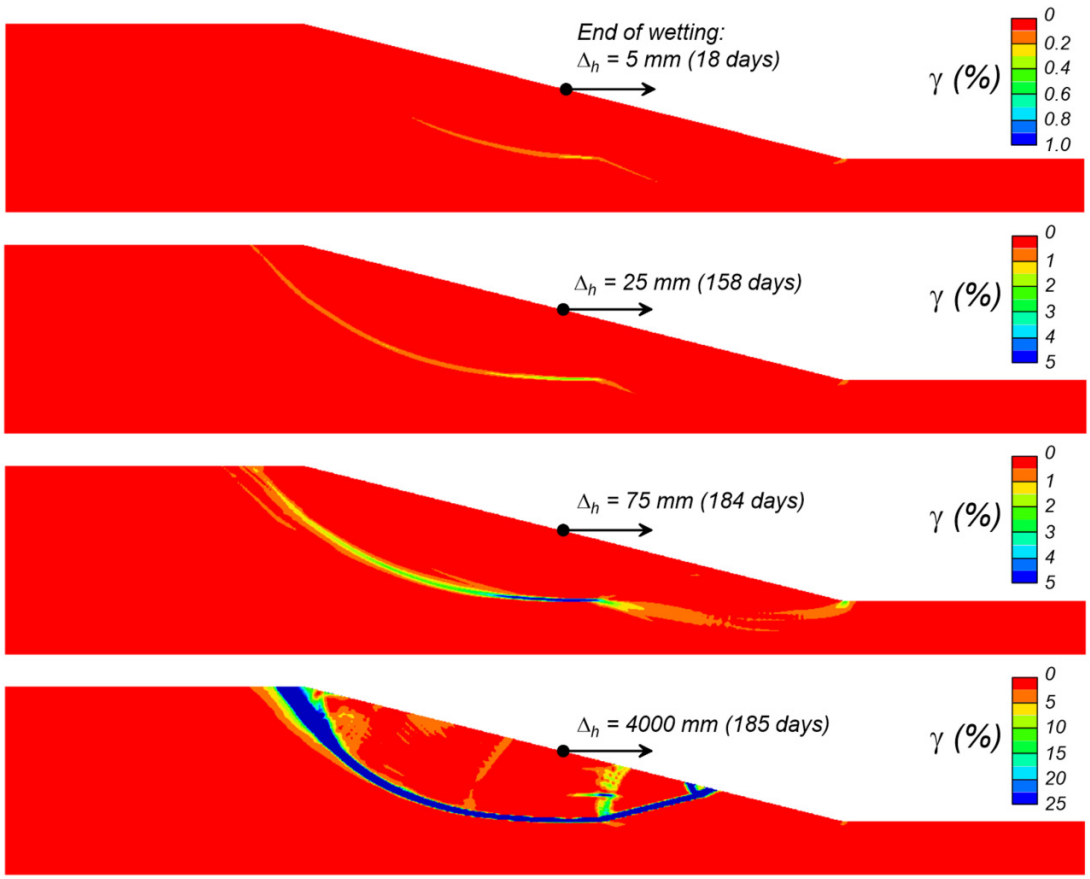

why the time to failure for the embankment (Fig. 14) was much longer than required for undrained creep rupture at the element level (Fig. 11). Softening elements shed shear stress into adjacent elements, which increased strain rates and hence increased shear resistances in all soils, thereby partially compensating for the reduced shear resistance in the softening elements. The elements adjacent to the strain-softening zones eventually developed enough creep-induced strain to begin strain-softening themselves. This process continued with the length of the softening zone progressively increasing over time, while slope displacements remained relatively small because the softening zone was relatively thin. This process progressed until further stress shedding led to instability with rapidly accelerating deformations.

The static stability of the slope in the absence of creep and progressive failure effects was evaluated using the strength reduction method with the same mesh and initial stress conditions and using non-strain softening Mohr Coulomb models. For long-term drained stability, the dike, tailings, and foundation materials were assigned effective friction angles of 34, 32, and 32 degrees, respectively. The factor of safety was 2.6 with the critical failure mechanism being shallow surface slides; deeper failure mechanisms reaching the tailings would have even greater factors of safety. For long-term (consolidated) undrained stability, the analyses assumed: (1) dike materials were drained with a friction angle of 34 degrees, (2) tailings were undrained where saturated with $s_u/\sigma'_{vc} = 0.27$ and drained where not saturated with a friction angle of 32 degrees, and (3) foundation clays were undrained with $s_u/\sigma'_{vc} = 0.50$. The factor of safety was 1.30 for this long-term consolidated, undrained loading condition, with the critical failure mechanism being approximately the same as the mechanism that developed in the creep analyses (Fig. 15). This margin of safety, based on s_u at reference strain rates, was insufficient to maintain stability under the combined influences of undrained creep, progressive failure, and modest wetting loads. For the analyses using Calibration B, the margin of safety was overcome largely by the combination of the static s_u at the slowest strain rates (i.e., $s_{u,ref}/s_{u,static} = 1/0.82 = 1.22$ per Fig. 6) and the $\Delta w_c = 13\%$ increasing the driving shear stresses in the tailings by about 7%. For the analyses using Calibration C, the smaller static s_u (i.e., $s_{u,ref}/s_{u,static} = 1/0.72 = 1.38$) meant that only a nominal wetting-induced load (e.g., $\Delta w_c = 2\%$) was sufficient to trigger the start of undrained creep leading to instability. For both calibrations, the delay between wetting-induced loading and slope instability was controlled by the progressive failure processes and strain rate at which the static s_u is reached.

Additional analyses were performed for different pool locations ($X_{pool} = 110$ m, 160 m, 210 m, and 260 m in Fig. 13), different calibrations, and a range of wetting-induced loads. Reducing the pool's distance from the dam crest reduced the static factor of safety (based on the above-described

strength reduction method), which reduced the amount of wetting-induced load required to trigger instability for any given calibration. Reducing the static s_u via calibration of the rate parameters also reduced the amount of wetting-induced loading required to trigger instability. The delay between wetting-induced loading and slope instability was most strongly dependent on the material rate dependency, the ratio of the static s_u to the s_u at reference strain rates, the static factor of safety, and magnitude of wetting-induced loads. The results of these sensitivity analyses were consistent with those described above and are consistent with expectations.

Other sensitivity analyses were performed to evaluate sensitivity to the mesh size and time step constraints. The analysis cases with Calibration B and $X_{pool} = 210$ m (Fig. 13) were repeated with the element sizes reduced by a factor of two in both directions (four times as many elements). Delayed slope instability developed 3 days after a wetting event with $\Delta w_c = 13\%$ versus after 23 days with the coarser mesh. Delayed slope instability developed 8 days after a wetting event with $\Delta w_c = 12\%$ versus the slope remaining stable with the coarser mesh. The slope remained stable for $\Delta w_c \leq 10\%$ versus remaining stable for $\Delta w_c \leq 12\%$ with the coarser mesh. Thus, the finer mesh reduced the magnitude of the loading event required to trigger a delayed failure, which is consistent with expected mesh effects for systems with strain-softening materials. Sensitivity analyses using smaller strain increment limits for constraining the time steps within the explicit creep solution procedure of FLAC showed less effect than the mesh size, with smaller shifts in the timing of delayed failures and no significant effect on the loading limits for stability. The sensitivity of the simulation results to mesh size and time steps introduces an additional uncertainty that must be considered in practice and represents common limitations in analyses involving strain-softening materials.

Discussion

The field scale analysis introduced herein highlighted the capabilities of the PM4SiltR model in a boundary value problem; however, it is important to be aware of potential limitations that may play a role in predicting the effects of undrained creep on slope stability. These creep analyses assumed fully undrained conditions in the tailings, which did not consider any potential beneficial effects from consolidation during creep. The potential for consolidation to progress fast enough to preclude undrained creep rupture may be assessed by evaluating their relative time scales, each of which involves considerable uncertainty in practice. These analyses also exhibited mesh sensitivity due to the strain-softening tendency of the material and the progressive failure localizing along a narrow band. However, the inclusion of viscoplasticity can provide a measure of regularization to partially offset the mesh sensitivity (Needleman 1988; Niazi et al. 2013; Oathes and Boulanger 2020, 2023). Additional study is needed into procedures to account for mesh dependency and regularization, the modeling of coupled consolidation and creep, and laboratory and field testing to determine applicable creep properties. Nonetheless, application of these analysis procedures utilizing PM4SiltR in a reevaluation of the 2019 Feijão Dam 1 failure provides an additional measure of validation for their use in engineering practice (Oathes and Boulanger 2022).

Delayed failures of seemingly stable embankments, such as seen in Feijão Dam 1, highlight the need to consider internal creep and strain rate-dependent shear strengths in analyses. Consideration of internal creep and strain rate-dependent shear strengths involves the calibration of advanced constitutive models that capture the viscoplastic tendencies of plastic silts and clays. Accurately modeling the viscoplastic behavior requires either more extensive laboratory testing than is commonly performed or reliance on empirical correlations. Estimates of rate-dependent material properties may be obtained from empirical correlations for soil types that are well represented in common correlations (e.g., Figs. 1 and 2), but these correlations are not well defined for many soils encountered in practice, including various tailings materials. Despite these challenges, the potential for undrained creep rupture needs to be considered in analysis or design. Recognizing the potential for creep and progressive failure can inform the selection of soil properties, assumptions for static liquefaction triggering, and appropriate factors of safety when performing limit equilibrium analyses. Alternatively, directly simulating creep and progressive failure in numerical analyses can provide insights for specific projects and provide a framework for developing generalized guidance.

Conclusion

The PM4SiltR model was developed to represent strain rate-dependent behaviors of clays and plastic silts in two-dimensional (plane strain) static slope stability applications. The model builds upon the stress ratio-controlled, critical state-compatible, bounding surface plasticity model PM4Silt. PM4SiltR was developed to simulate strain rate-dependent shear strength, stress relaxation, and creep; it is unable to simulate strain rate-dependent consolidation behavior because the model does not have a cap. The non-viscous behavior of PM4SiltR follows the monotonic behavior of PM4Silt. Six parameters were introduced to control the viscous behavior. The model utilizes a consistency approach wherein the CSL and the critical state stress ratio are made strain-rate dependent. A static yield surface separates the viscous and non-viscous behaviors at slow or zero loading rates. Transient responses and stress relaxation are controlled by an internal strain rate and auto-decay process. The model framework facilitates efficient calibration against empirical correlations or site-specific testing data for those mechanisms most important to slope stability applications, while accepting certain approximations and limitations in representing underlying fundamental mechanisms under more generalized loading conditions.

Single element simulations of undrained DSS shearing and undrained creep illustrated the constitutive response of the model. The introduced viscoplasticity was shown to increase the peak strength and the strain at the mobilization of peak strength as the applied strain rate increases. The

peak strength became strain-rate independent at strain rates smaller than the minimum strain rate defining the static bounding surface. Simulations of DSS undrained creep were either stable or ruptured depending on the magnitude of the imposed stress level and the static bounding surface. Lower sustained shear stresses typically resulted in stable conditions and higher sustained stresses resulted in rupture, with the time to rupture decreasing with increasing sustained stresses. Stress conditions close to the bounding surface may result in small magnitudes of induced creep strain before becoming stable and ceasing deformation.

PM4SiltR was used to simulate undrained creep rupture in a hypothetical tailings dam with a strain-softening material. Small changes in loading were shown to be able to trigger a progressive failure due to undrained creep rupture in the strain-softening material resulting in delayed slope instability. Simulations showed that minor changes in phreatic surface elevation or pool length could transition an embankment from stable to unstable in the long term. Similarly, wetting events were shown to be capable of causing sufficient internal strain to trigger undrained creep rupture, progressive failure, and slope instability.

The ability to incorporate viscous effects into analyses of earthen structures founded on or containing clays or plastic silts can improve confidence in analysis results by better representing the soil mechanics behaviors observed in the laboratory or in situ. Further advancing the modeling of creep and progressive failure in practice requires further investigation into mesh effects, site-specific testing, and empirical relations for viscous soil properties, as well as the relationship between creep and consolidation. Despite the remaining challenges, the numerical and constitutive modeling approach herein shows promise as a way for directly accounting for creep and progressive failure in applications or in studies to develop generalized guidance.

Acknowledgements

Portions of the work were supported by the California Department of Water Resources under Contract 4600009751. Any opinions, findings, or recommendations expressed herein are those of the authors and do not necessarily represent the views of this organization. The authors appreciate the above support.

Article information

History dates

Received: 29 September 2022
Accepted: 20 January 2024
Accepted manuscript online: 27 January 2024
Version of record online: 16 September 2024

Copyright

Data availability

Data that support the findings of this study are available from the corresponding author upon reasonable request.

Author information

Author ORCIDs

Tyler J. Oathes https://orcid.org/0000-0002-3496-0080
Ross W. Boulanger https://orcid.org/0000-0002-2518-901X
Katerina Ziotopoulou https://orcid.org/0000-0001-5494-497X

Author notes

Katerina Ziotopoulou served as an Editorial Board Member at the time of manuscript review and acceptance; peer review and editorial decisions regarding this manuscript were handled by another Editorial Board Member.

Author contributions

Conceptualization: TJO, RWB
Data curation: TJO, RWB
Formal analysis: TJO, RWB
Funding acquisition: RWB
Investigation: TJO, RWB
Methodology: TJO, RWB, KZ
Project administration: RWB
Resources: RWB, KZ
Software: RWB, KZ
Supervision: RWB
Validation: TJO, RWB, KZ
Visualization: TJO, RWB
Writing – original draft: TJO, RWB, KZ
Writing – review & editing: TJO, RWB, KZ

Competing interests

The authors declare there are no competing interests.

References

Boulanger, R.W., and Ziotopoulou, K. 2017. PM4Sand (Version 3.1): a sand plasticity model for earthquake engineering applications. Report No. UCD/CGM-17-01, Center for Geotechnical Modeling, Department of Civil and Environmental Engineering, University of California, Davis, CA.

Boulanger, R.W., and Ziotopoulou, K. 2019. A constitutive model for clays and plastic silts in plane-strain earthquake engineering applications. Soil Dynamics and Earthquake Engineering, **127**(2019): 105832. doi:10.1016/j.soildyn.2019.105832.

Boulanger, R.W., Ziotopoulou, K., and Oathes, T.J. 2022. PM4SiltR (Version 1): a silt plasticity model with rate effects for slope stability applications. Report No. UCD/CGM-21/04, Center for Geotechnical Modeling, University of California, Davis, CA.

Clarke, S.D., and Hird, C.C. 2012. Modelling of viscous effects in natural clays. Canadian Geotechnical Journal, **49**: 129–140. doi:10.1139/t11-084.

Diaz-Rodriguez, J.A., Martinez-Vasquez, J.J., and Santamarina, J.C. 2009. Strain-rate effects in Mexico City soil. Journal of Geotechnical and Geoenvironmental Engineering, **135**(2): 300–305.

Duvaut, G., and Lions, J.L. 1972. Les Inequations en Mechanique et en Physique. Dunod, Paris.

Graham, K., Crooks, J., and Bell, A. 1983. Time effects on the stress-strain behaviour of natural soft clays. Géotechnique, **33**(3): 327–340. doi:10.1680/geot.1983.33.3.327.

Gylland, A.S., Jostad, H.P., and Nordal, S. 2014. Experimental study of strain localization in sensitive clays. Acta Geotechnica, **9**: 227–240. doi:10.1007/s11440-013-0217-8.

Itasca. 2019. Fast Lagrangian Analysis of Continua (FLAC), release 8.1. Itasca Consulting Group, Inc., Minneapolis, MN.

Jiang, J., Ling, H.I., Kaliakin, V.N., Zeng, X., and Hung, C. 2017. Evaluation of an anisotropic elastoplastic-viscoplastic bounding surface model for clays. Acta Geotechnica, **12**: 335–348. doi:10.1007/s11440-016-0471-7.

Kiernan, M., and Montgomery, J. 2018. Numerical simulations of the fourth avenue landslide considering strain-softening. *In* Proceedings of Geotechnical Earthquake Engineering and Soil Dynamics V, Geotechnical Special Publication 290, *Edited by* S.J. Brandenberg and M.T. Manzari. ASCE, New York, NY. 67–78.

Kulhawy, G.H., and Mayne, P.W. 1990. Manual on estimating soil properties for foundation design. Report EPRI EL-6800, Electric Power Research Institute, Palo, Alto, CA.

Kutter, B.L., and Sathialingam, N. 1992. Elastic-viscoplastic modelling of the rate-dependent behaviour of clays. Géotechnique. **42**(3): 427–441. doi:10.1680/geot.1992.42.3.427.

Lacerda, W. 1976. Stress-relaxation and creep effects on soil deformation. University of California, Berkeley, CA.

Ladd, C.C., and DeGroot, D.J. 2004. Recommended practice for soft ground site characterization: Arthur Casagrande Lecture. 12th Panamerican Conference on Soil Mechanics and Engineering. MIT, Cambridge, MA.

Lefebvre, G., and LeBoeuf, D. 1987. Rate effects and cyclic loading of sensitive clays. Journal of Geotechnical Engineering, **113**(5): 476–489. doi:10.1061/(ASCE)0733-9410(1987)113:5(476).

Leroueil, S. 2006. The isotache approach. Where are we 50 years after its development by Professor Suklje? 2006 Prof. Suklje's Memorial Lecture.

Leroueil, S., Tavenas, F., Samson, L., and Morin, P. 1983. Preconsolidation pressure of Champlain clays. Part II. Laboratory determination. Canadian Geotechnical Journal, **20**: 803–816. doi:10.1139/t83-084.

Martindale, H., Chakraborty, T., and Basu, D. 2012. A rate dependent constitutive model for clay. *In* Proceedings of GeoCongress 2012: State of the Art and Practice in Geotechnical Engineering. pp. 859–868.

Meehan, C.L., Boulanger, R.W., and Duncan, J.M. 2008. Dynamic centrifuge testing of slickensided shear surfaces. Journal of Geotechnical and Geoenvironmental Engineering, ASCE, **134**(8): 1086–1096. doi:10.1061/(ASCE)1090-0241(2008)134:8(1086).

Mun, W., Teixeira, T., Balci, M.C., Svoboda, J., and McCartney, J.S. 2016. Rate effects on the undrained shear strength of compacted clay. Soils and Foundations, **56**(4): 719–731. doi:10.1016/j.sandf.2016.07.012.

Needleman, A. 1988. Material rate dependence and mesh sensitivity in localization problems. Computer Methods in Applied Mechanics and Engineering, **67**: 69–85. doi:10.1016/0045-7825(88)90069-2.

Niazi, M.S., Wisselink, H.H., and Meinders, T. 2013. Viscoplastic regularization of local damage models: Revisited. Computational Mechanics, **51**(2): 203–216. doi:10.1007/s00466-012-0717-7.

Oathes, T.J. 2022. Accounting for viscous effects in nonlinear analyses of strain softening clays. Dissertation. University of California, Davis, CA.

Oathes, T.J., and Boulanger, R.W. 2020. Influence of strain rate on localization and strain-softening in normally consolidated clays with varying strength profiles. Geo-Congress 2020: Modeling, Geomaterials, and Site Characterization. Geotechnical Special Publication, Vol. **317**. *Edited by* J. P. Hambleton, R. Makhnenko and A. S. Budge. ASCE. pp. 247–255.

Oathes, T.J., and Boulanger, R.W. 2022. Nonlinear viscoplastic modeling of the Feijão Dam 1 failure. Geo-Congress 2022: State of the Art and Practice in Geotechnical Engineering. ASCE, Charlotte, NC. March 20-23, 2022.

Oathes, T.J., and Boulanger, R.W. 2023. Effect of viscoplasticity on localization in saturated clays and plastic silts. Journal of Geotechnical and Geoenvironmental Engineering, **149**(4): 04023016. doi:10.1061/JGGEFK.GTENG-10984.

Perzyna, P. 1963. The constitutive equations for rate sensitive plastic materials. Quarterly Applied Mathematics, **20**: 321–332.

Peuchen, J., and Mayne, P.W. 2007. Rate effects in vane shear testing. In Proceedings of the 6th International Offshore Site Investigation and Geotechnics Conference: Confronting New Challenges and Sharing Knowledge. pp. 259–265.

Rezania, M., Taiebat, M., and Poletti, E. 2016. A viscoplastic SANICLAY model for natural soft soils. Computers and Geotechnics., **73**: 128–141. doi:10.1016/j.compgeo.2015.11.023.

Robertson, P.K., Melo, L., Williams, D.J., and Wilson, G.W. 2019. Report of the expert panel on the technical causes of the failure of Feijao Dam 1.

Santamarina, J.C., and Shin, H. 2009. Friction in granular media. Mesoscale shear physics in earthquake and landslide mechanics. CRC Press, London. pp. 157–188.

Sheahan, T.C. 1995. Interpretation of undrained creep tests in terms of effective stresses. Canadian Geotechnical Journal, **32**: 373–379. doi:10.1139/t95-038.

Sheahan, T.C., Ladd, C.C., and Germaine, J.T. 1996. Rate-dependent undrained shear behavior of saturated clay. Journal of Geotechnical Engineering, **122**(2): 99–108. doi:10.1061/(ASCE)0733-9410(1996)122:2(99).

Shi, Z., and Hambleton, J.P. 2019. Bounding surface elasto-viscoplasticity: a general constitutive framework for rate-dependent geomaterials. Journal of Engineering Mechanics, **145**(3): 04019002. doi:10.1061/(ASCE)EM.1943-7889.0001578.

Silvestri, V., Soulie, M., Touchan, Z., and Fay, B. 1988. Triaxial relaxation tests on a soft clay. *In* Advanced triaxial testing of Soil and Rock, *Edited by* R. Donaghe, R. Chaney and M. Silver. ASTM International, West Conshohocken, PA. pp. 321–337. doi:10.1520/STP29084S.

Singh, A., and Mitchell, J.K. 1968. General stress-strain-time function for soils. Journal of the Soil Mechanics and Foundations Division, **94**(1): 21–46. doi:10.1061/JSFEAQ.0001084.

Skempton, A.W. 1985. Residual strength of clays in landslides, folded strata, and the laboratory. Géotechnique, **35**(1): 3–18. doi:10.1680/geot.1985.35.1.3.

Sorenson, K.K., Baudet, B.A., and Simpson, B. 2007. Influence of structure on the time-dependent behaviour of a stiff sedimentary clay. Géotechnique, **57**(1): 113–124. doi:10.1680/geot.2007.57.1.113.

Vaid, Y.P., Robertson, P.K., and Campanella, R.G. 1979. Strain rate behaviour of Saint-Jean-Vianney Clay. Canadian Geotechnical Journal, **16**: 34–42. doi:10.1139/t79-004.

Wang, W.M., Sluys, L.J., and De Bort, R. 1997. Viscoplasticity for instabilities due to strain softening and strain rate softening. International Journal for Numerical Methods in Engineering, **40**: 3839–3864. doi:10.1002/(SICI)1097-0207(19971030)40:20%3c3839::AID-NME245%3e3.0.CO;2-6.

Watabe, Y., Udaka, K., Nakatani, Y., and Leroueil, S. 2012. Long-term consolidation behavior interpreted with isotache concept for worldwide clays. Soils and Foundations, **52**(3): 449–464. doi:10.1016/j.sandf.2012.05.005.

Wedage, A.M.P., Morgenstern, N.R., and Chan, D.H. 1998. A strain rate dependent constitutive model for clays at residual strength. Canadian Geotechnical Journal, **35**(2): 364–373. doi:10.1139/t97-085.

Yin, Z.Y., Hicher, P.Y., Riou, Y., and Huang, H.W. 2006. An elasto-viscoplastic model for soft clay. *In* Proceedings of GeoShanghai International Conference 2006. Shanghai, China. pp. 312–319.

Yin, Z.Y., Karstunen, M., Chang, C.S., Koskinen, M., and Lojander, M. 2011. Modeling time-dependent behavior of soft sensitive clay. JGGE. **137**(11): 1103–1113.

Yin, Z.Y., Xu, Q., and Yu, C. 2015. Elastic-viscoplastic modeling for natural soft clays considering nonlinear creep. International Journal of Geomechanics, **15**(5): A6014001. doi:10.1061/(ASCE)GM.1943-5622.0000284.

Yuan, Y., and Whittle, A.J. 2018. A novel elasto-viscoplastic formulation for compression behaviour of clays. Géotechnique, **68**(12): 1044–1055. doi:10.1680/jgeot.16.P.276.

Yuan, Y., and Whittle, A.J. 2020. Formulation of a new elastoviscoplastic model for time-dependent behavior of clay. International Journal for Numerical and Analytical Methods in Geomechanics. **45**(5): 700–716. doi:10.1002/nag.3173.

Zergoun, M., and Vaid, Y.P. 1994. Effective stress response of clay to undrained cyclic loading. Canadian Geotechnical Journal, **31**(5): 714–727. doi:10.1139/t94-083.

Ziotopoulou, K., and Boulanger, R.W. 2016. Plasticity modeling of liquefaction effects under sloping ground and irregular cyclic loading con-

ditions. Soil Dynamics and Earthquake Engineering, **84**(2016): 269–283. doi:10.1016/j.soildyn.2016.02.013.

Appendix A

A pseudo-code for the implementation of PM4SiltR in FLAC 8.1 is provided below. This pseudocode describes the sequence of calculations for both the model and its implementation within the explicit, finite difference, mixed formulation of FLAC. The mixed discretization formulation of FLAC uses four overlaying triangular elements within each quadrilateral zone, as illustrated in Fig. A.1. The implementation of PM4SiltR is similar to those for other constitutive models within FLAC, except that the complexity of the bounding surface formulation with its various history terms required specific attention to zone-averaging procedures and numerical corrections to ensure consistency is satisfied by zone-averaged variables. The pseudocode emphasizes the calculation of strain rate-dependent variables unique to PM4SiltR. Additional details of the implementation scheme for the parent model PM4Silt in the mixed formulation of FLAC are provided in Boulanger and Ziotopoulou (2019).

Operations within one subzone:

1. Initialize the model parameters; this only happens when the model is first assigned or when FirstCall is set to zero at some point during the analysis. For detailed information on what parameters are initialized (or reset), see Boulanger and Ziotopoulou (2019).
2. Obtain the strain increment from FLAC $d\boldsymbol{\varepsilon}$.
3. Decompose the strain increment into volumetric and deviatoric components, $d\varepsilon_p$ and $d\varepsilon_s$.
4. Calculate the trial elastic stress increment and trial elastic stress:

$$\boldsymbol{\sigma}_{tr} = \boldsymbol{\sigma}_0 + d\boldsymbol{\sigma}_{tr} = \boldsymbol{\sigma}_0 + 2Gd\boldsymbol{\varepsilon}_s + Kd\varepsilon_p\boldsymbol{I}$$

5. Calculate the trial stress ratio $\boldsymbol{r_{tr}}$, the distance from the yield surface *dist*, the unit normal to the yield surface $\boldsymbol{n}$, and the inner product of the change in back-stress ratio tensor α with unit normal vector *daxn*.

$$\begin{aligned}
\boldsymbol{r}_{tr} &= \frac{\boldsymbol{\sigma}_{tr} - p_{tr}\boldsymbol{I}}{p_{tr}} \\
dist &= \sqrt{(\boldsymbol{r}_{tr} - \boldsymbol{\alpha}_0) : (\boldsymbol{r}_{tr} - \boldsymbol{\alpha}_0)} \\
\boldsymbol{n} &= \frac{(\boldsymbol{r}_{tr} - \boldsymbol{\alpha}_0)}{dist} \\
daxn &= (\boldsymbol{\alpha}_0 - \boldsymbol{\alpha}_{in}) : \boldsymbol{n}
\end{aligned}$$

6. Check for yield:
   a. If elastic, then commit the trial stresses. Go to step 8.

$$\begin{aligned}
dist &< \frac{1}{\sqrt{2}}m \\
\boldsymbol{\sigma}_0 &= \boldsymbol{\sigma}_{tr}
\end{aligned}$$

   b. If inelastic:
      i. Calculate loading index L:

$$L = \frac{2G\boldsymbol{n} : d\boldsymbol{e} - \boldsymbol{n} : \boldsymbol{r}Kd\varepsilon_v}{K_p + 2G - KD\boldsymbol{n} : \boldsymbol{r}}$$

      ii. Calculate trial stress increment and trial stress:

$$\begin{aligned}
\boldsymbol{\sigma}_{tr} = \boldsymbol{\sigma}_0 + d\boldsymbol{\sigma}_{tr} = \boldsymbol{\sigma}_0 + 2Gd\boldsymbol{\varepsilon}_s \\
+Kd\varepsilon_p\boldsymbol{I} - L\{2G\boldsymbol{n} + KD\boldsymbol{I}\}
\end{aligned}$$

      iii. Apply penalties to stress ratios and back-stress ratios to meet the consistency condition and to remain within the greater of the bounding and dilatancy surfaces.
      iv. Calculate image back-stress ratios and inner products:

$$\begin{aligned}
\boldsymbol{\alpha}^b &= \sqrt{1/2}\left[M^b - m\right]\boldsymbol{n} \\
\boldsymbol{\alpha}^d &= \sqrt{1/2}\left[M^d - m\right]\boldsymbol{n} \\
\boldsymbol{\alpha}^{dR} &= \sqrt{1/2}\left[M^{dR} - m\right]\boldsymbol{n}
\end{aligned}$$

      v. Commit the trial stresses (back-stress ratios, stress ratio, and mean stress, stress)
7. Return all stress tensor components to FLAC (at this point, FLAC takes over and will average them according to the mixed discretization scheme)

Operations referring to the whole zone:

8. After the calculation has completed the 4th subzone, the following additional calculations are performed for the overall zone. Recall the following parameters for all four subzones and compute area-weighted average values for:
   - Volumetric strain increment $d\bar{\varepsilon}_p$
   - Deviatoric increment $d\bar{\boldsymbol{\varepsilon}}$ and deviatoric strain rate $d\left(\dot{\bar{\gamma}}\right)$
   - Mean stress $\bar{p}$
   - Stress tensor (committed one) $\bar{\boldsymbol{\sigma}}_0$
   - Back-stress ratio tensor $\bar{\boldsymbol{\alpha}}_0$
   - Unit normal to yield surface vector $\bar{\boldsymbol{n}}$
9. Apply penalties to the averaged zone parameters to meet the consistency condition and maintain the yield surface inside the greater of the bounding and dilatancy surfaces.
10. Calculate image back-stress ratios and inner products for the averaged zone parameters.
11. Calculate *daxn* for the averaged zone parameters and determine whether a loading reversal has occurred.
12. Compute Dilatancy D and Plastic Modulus K_p for the past average step in the zone.
13. Compute plastic volumetric strain for use in fabric terms.
14. If $(\boldsymbol{\alpha}^d - \boldsymbol{\alpha}) : \boldsymbol{n} < 0$, update the fabric tensor for the zone and if exceeding its former value, update the cumulative fabric term.
15. Update the strain-rate-dependent parameters M and e_{1kPa} as

$$\begin{aligned}
M &= M_{ref}\left(1 + F_M \log\left(\frac{\dot{\bar{\gamma}}}{\dot{\gamma}_{ref}} + R_{\dot{\gamma},\min}\right)\right) \\
e_{1kPa} &= e_{1kPa,ref} - \lambda \cdot \ln\left(1 + F_p \log\left(\frac{\dot{\bar{\gamma}}}{\dot{\gamma}_{ref}} + R_{\dot{\gamma},\min}\right)\right)
\end{aligned}$$

Fig. A.1. Schematic illustration of the averaging procedure followed in the implementation of PM4SiltR: zone-averaged values are computed for some internal variables of the model, denoted as m, at the end of each explicit time step, after which other internal parameters, denoted as q, are computed based on the zone-averaged parameters (Boulanger and Ziotopoulou 2019).

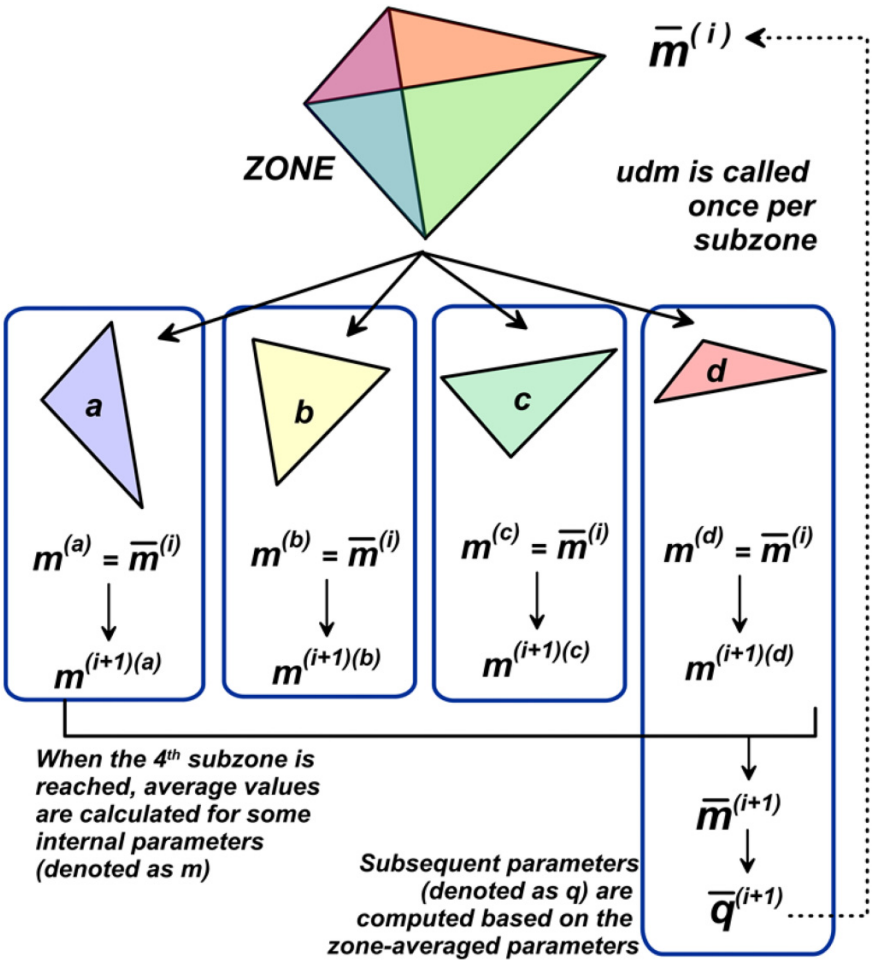

16. Update the state parameter and the bounding and dilatancy stress ratios.
17. Apply relaxation to stresses and, if needed, apply correction to back-stress to satisfy consistency condition.
18. Update the elastic shear modulus (depends on fabric) and the elastic bulk modulus for the next step.
19. Update the initial and previous initial back-stress values and the strain increment accumulators.
20. Update initial back-stress ratios upon reversal.
21. Commit zone stress tensor, zone mean stress, zone back-stress ratio tensor, and zone stress ratio tensor to memory.